Electronic Supplementary Material for Level Set Simulation Methodology

Anup Basak and Anurag Gupta*

Department of Mechanical Engineering, Indian Institute of Technology, Kanpur 208016, India

May 8, 2014

The purpose of this supplement is to provide details of the numerical scheme that we have used in studying the problem of coupled grain boundary (GB) motion in the main paper. Our simulations are based on the local level set method of Peng et al. [11], which is a modification of the classical level set method [10, 13], combined with discretization and reinitialization schemes of Jiang and Peng [7], Russo and Smereka [12], and Smereka [14]. We have tailored the numerical schemes for problems related to GB motion. We also provide several examples to verify our numerical procedure, including surface diffusion driven by Laplacian of curvature, Wulff shape, and shrinkage of grains with anisotropic GB energy. Other simulations, in particular those involving coupled motion and anisotropic kinetic coefficients are provided in the main paper. The notation in this note is consistent with the main text.

1 Introduction

We begin with a GB energy of the form [2]

$$\gamma(\phi, \kappa) = \gamma_c(\phi) + \frac{1}{2}\delta_r \kappa^2, \tag{1.1}$$

where ϕ represents the orientation of the two-dimensional GB, κ is the curvature, and $\delta_r << 1$ is the regularization parameter. The misorientation dependence of γ_c has been dropped for convenience. The governing equation for GB normal motion is given by [3]

$$V = -M(\nabla \cdot \boldsymbol{\xi} + \delta_r(\Delta^S \kappa + 1/2\kappa^3)), \tag{1.2}$$

where M is the mobility of the boundary and $\boldsymbol{\xi}$ is the Cahn-Hoffman vector given by

$$\boldsymbol{\xi} = \gamma_c \boldsymbol{n} - \gamma_c' \boldsymbol{t}, \tag{1.3}$$

with γ_c' denoting the derivative of γ_c w.r.t. ϕ, and $\boldsymbol{n}$ and $\boldsymbol{t}$ are unit normal and tangent to the GB (see Fig. 2(b)). The term $\nabla \cdot \boldsymbol{\xi}$ stands for the divergence of $\boldsymbol{\xi}$ and Δ^S for the surface Laplacian

*ag@iitk.ac.in

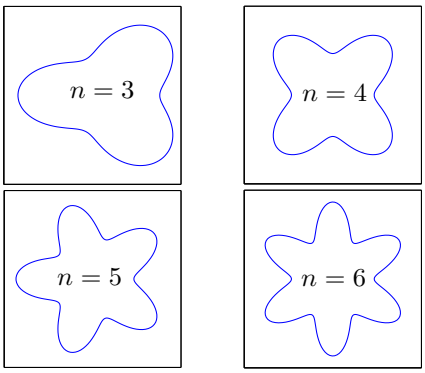

Figure 1: Polar plots of γ_c given by Eq. (1.4) for different n indicated in the figure.

operator. The surface gradient of a scalar field g, defined on a surface C with normal $\boldsymbol{n}$, is given as a vector field $\nabla^S g = \mathbb{P}\nabla g$, where $\mathbb{P} = \mathbf{1} - \boldsymbol{n} \otimes \boldsymbol{n}$ is the projection tensor and $\mathbf{1}$ is the identity tensor. The surface divergence of a vector field $\boldsymbol{g}$ on C is defined as $\nabla^S \cdot \boldsymbol{g} = \text{trace}(\nabla^S \boldsymbol{g})$. The surface Laplacian of g is a scalar field defined as $\Delta^S g = \nabla^S \cdot (\nabla^S g)$. That the relation (1.2) is same as that derived in the main paper (but restricting to normal motion) can be seen by first noting that $\nabla^S \cdot \boldsymbol{\xi} = \nabla \cdot \boldsymbol{\xi}$ (see Ch. 1 of [5] for proof) and then writing $\nabla^S \cdot \boldsymbol{\xi}$ as $\frac{\partial \boldsymbol{\xi}}{\partial s} \cdot \boldsymbol{t}$ for the closed GB of our consideration. Moreover, $\Delta^s \kappa$ is simply $\partial^2 \kappa / \partial s^2$.

For the purpose of this supplement, we assume the form for smooth anisotropic boundary energy as [16]

$$\gamma_c = 1 - \alpha_e \cos(n\phi), \tag{1.4}$$

where n is an integer and $0 < \alpha_e < 1$ is a phenomenological constant determining the degree of anisotropy. The nature of this energy is represented in the polar plots shown in Figure 1 for different n.

There are two major challenges associated with solving the problem of boundary motion with anisotropic boundary energy having curvature regularization. The first term on the R.H.S. of (1.2) introduces backward parabolicity in the PDE, since $\gamma_c(\phi)$ is generally non-convex [2]. This leads to unstable solutions in the absence of regularization, i.e., $\delta_r = 0$. The introduction of the regularization term however raises the order of the PDE to four in space variables due to the presence of the surface Laplacian of κ in (1.2). The higher order derivatives are very sensitive to errors in κ during numerical computations, thereby requiring special treatment. Here we have followed the scheme proposed by Smereka [14] for computing $\Delta^S \kappa$. To verify our computations, we have simulated surface diffusion driven by surface Laplacian of the mean curvature for an elliptic and a star shaped crystal. We also verify our numerical scheme when both $\nabla \cdot \boldsymbol{\xi}$ and the regularization terms are present. To do so, we consider problems involving normal motion of closed boundaries. This includes recovering the Wulff shapes for isolated crystal with free boundaries, and studying the shrinkage of isolated GBs (without any GB junction).

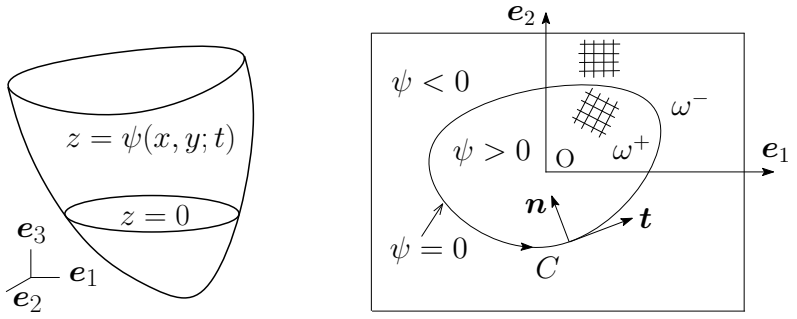

(a) (b)

Figure 2: (a) The zero level set (the curve with $z = 0$) embedded in a higher dimensional surface $z = \psi(x, y; t)$ where $\boldsymbol{x} = x\boldsymbol{e}_1 + y\boldsymbol{e}_2$. (b) C, which is the zero level set, represents a smooth closed GB with the inward normal $\boldsymbol{n}$ and a tangent $\boldsymbol{t}$ in the direction of increasing arc length.

2 Level set method and numerical schemes

Level set method is a numerical technique which was developed by Osher and Sethian [10] to study the evolution of moving boundaries. Within the present context, GB is considered to be the zero level curve of a function $\psi(\boldsymbol{x}, t)$, as shown in Figure 2, where ψ is initialized as a signed distance function (SDF) such that it is positive inside of ω^+ and negative outside (cf. Ch. 2 of [9]). By choosing a parametrization such that $\boldsymbol{n}$ points in the direction of increasing ψ, we obtain the following expressions for the normal, tangent, and curvature [9]

$$\boldsymbol{n} = \frac{\partial\psi/\partial x}{||\nabla\psi||}\boldsymbol{e}_1 + \frac{\partial\psi/\partial y}{||\nabla\psi||}\boldsymbol{e}_2, \tag{2.1}$$

$$\boldsymbol{t} = \frac{\partial\psi/\partial y}{||\nabla\psi||}\boldsymbol{e}_1 - \frac{\partial\psi/\partial x}{||\nabla\psi||}\boldsymbol{e}_2, \text{ and} \tag{2.2}$$

$$\kappa = -\nabla\cdot\left(\frac{\nabla\psi}{||\nabla\psi||}\right). \tag{2.3}$$

For a given boundary normal velocity V, ψ is updated w.r.t. time in the whole domain ω using the following Hamilton-Jacobi equation (cf. Ch. 3 of [9])

$$\frac{\partial\psi}{\partial t} + V\,||\nabla\psi|| = 0. \tag{2.4}$$

The updated level set curve, given by $\psi = 0$, which gives the new location for the GB, is then captured by interpolations. Hence it is a front capturing method, rather than a front tracking method.[1]

[1]In the front tracking method, the interfaces (or boundaries) themselves are discretized and evolved under the governing kinetic laws. It is computationally cheap, but has many other inherent drawbacks as discussed by Sethian in Ch. 2 of [13].

A computationally less expensive local level set scheme, proposed by Peng at el. [11], alternatively updates the level set function only in a small neighborhood of the zero level set by making use of the modified Hamilton-Jacobi equation

$$\frac{\partial \psi}{\partial t} + c(\psi) V_{\text{ext}} ||\nabla \psi|| = 0, \tag{2.5}$$

where $c(\psi)$ is a cut-off function introduced to ensure that ψ is updated only in a narrow region surrounding $\psi = 0$ and V_{ext} is the extended normal velocity. Following [11], we take the cut-off function as

$$c(\psi) = \begin{cases} 1, & \text{if } |\psi| \le c_1 \\ (|\psi| - c_2)^2 (2|\psi| + c_2 - 3c_1)/(c_2 - c_1)^3, & \text{if } c_1 < |\psi| \le c_2 \\ 0, & \text{if } |\psi| > c_2, \end{cases} \tag{2.6}$$

where c_1 and $c_2 (> c_1)$ are constants such that the computational domain in divided into two tubes $|\psi| \le c_1$ and $|\psi| \le c_2$, denoted by T_1 and T_2, respectively. The cut-off function is unity within the tube $|\psi| \le c_1$, reducing smoothly to zero at the boundary of T_2. On the other hand we can construct extension q_{ext} of a given field q by solving the hyperbolic PDE [11]

$$\frac{\partial q}{\partial t} + (\operatorname{sign} q)(\boldsymbol{n} \cdot \nabla q) = 0. \tag{2.7}$$

The steady state solution of this equation is taken as q_{ext}. It satisfies $q_{\text{ext}} = q$ on C and remains constant along the normal to C. This follows from observing that the direction of ∇q is perpendicular to the normal to C, since we want constant q curves to lie parallel to the normal vector; hence $\boldsymbol{n} \cdot \nabla q = 0$. We use this procedure to evaluate the extension V_{ext} of V.

After solving (2.5), the updated ψ will not necessarily remain an SDF [11]. This is resolved by reinitializing ψ to an SDF by solving (locally) the PDE [11]

$$\frac{\partial d}{\partial t} + (\operatorname{sign} d_i)(||\nabla d|| - 1) = 0, \tag{2.8}$$

such that $d_i = d(\boldsymbol{x}, 0) = \psi(\boldsymbol{x}, t)$, i.e. the initial condition for (2.8) is the solution of (2.5). The steady state solution of (2.8), which solves the special form of the Eikonel equation $||\nabla d|| = 1$, will be an SDF.

During reinitialization the zero level set remains stationary, but other level curves (contours) in the neighborhood of C move with unit speed (with proper sign) along the characteristics in the normal direction, and converge to an SDF in the neighborhood of the interface of width Δt around C after one iteration, where Δt is the time step for updating reinitialization equation. Following Peng et al. [11], we take

$$\operatorname{sign} d = \frac{d}{\sqrt{d^2 + (||\nabla d|| h)^2}}, \tag{2.9}$$

where h is the mesh size. The second term under the square root in (2.9) has been added to avoid division by zero.

2.1 Discretization

2.1.1 Hamilton-Jacobi equation

We use the method of lines to solve (2.5) and (2.8). We start by discretizing (2.5) in space and then integrate the resulting system of ODEs with respect to time [13]. For spatial discretization, we use the upwind finite difference scheme (cf. Ch. 6 of [13]). The domain ω is discretized uniformly along $\boldsymbol{e}_1$ and $\boldsymbol{e}_2$ directions with N number of grid points and a mesh size given by h. Let (x_i, y_j) be the $(i,j)_{th}$ node in the 2D lattice grid. At time t_n and at the $(i,j)_{th}$ node, we denote the level set function by $\psi^n_{i,j}$, occasionally omitting the superscript n when the time is fixed.

The semi-discrete form of (2.5) is given as

$$\frac{d\psi_{i,j}}{dt} = L(\boldsymbol{x}, \psi^{\pm}_{x\,i,j}, \psi^{\pm}_{y\,i,j}, \kappa_{i,j}, \boldsymbol{n}_{i,j}, \dot{\theta}), \tag{2.10}$$

where $L = -cV_{\text{ext}}||\nabla\psi||$. The discretized form of L is

$$L_{i,j} = -\max((cV_{\text{ext}})_{i,j}, 0)||\nabla^+\psi||_{i,j} - \min((cV_{\text{ext}})_{i,j}, 0)||\nabla^-\psi||_{i,j}, \tag{2.11}$$

where

$$||\nabla^{\pm}\psi||_{i,j} = [\max(\psi^{\mp}_{x\,i,j}, 0)^2 + \min(\psi^{\pm}_{x\,i,j}, 0)^2 + \max(\psi^{\mp}_{y\,i,j}, 0)^2 + \min(\psi^{\pm}_{y\,i,j}, 0)^2]^{1/2}. \tag{2.12}$$

To compute $\psi^{\pm}_{x\,i,j}$ and $\psi^{\pm}_{y\,i,j}$, a fifth order weighted essentially non-oscillatory (WENO) scheme [7] has been used. This higher order scheme ensures good numerical accuracy in computing the spatial derivatives while solving the Hamilton-Jacobi equation and the reinitialization equation. The spatial discretization of the fifth order WENO scheme is briefly outlined below (see [7] for details).

Introduce

$$\begin{aligned} \Delta^+_x\psi_{i,j} &= \psi_{i+1,j} - \psi_{i,j}, \quad \Delta^-_x\psi_{i,j} = \psi_{i,j} - \psi_{i-1,j}, \\ \Delta^+_y\psi_{i,j} &= \psi_{i,j+1} - \psi_{i,j}, \quad \Delta^-_y\psi_{i,j} = \psi_{i,j} - \psi_{i,j-1} \end{aligned} \tag{2.13}$$

to define

$$\begin{aligned} \psi^{\pm}_{x\,i,j} &= \frac{1}{12\,h}\left(-\Delta^+_x\psi_{i-2,j} + 7\Delta^+_x\psi_{i-1,j} + 7\Delta^+_x\psi_{i,j} - \Delta^+_x\psi_{i+1,j}\right) \\ &\quad \pm\Phi^{\text{WENO}}\left(\frac{\Delta^-_x\Delta^+_x\psi_{i\pm2,j}}{h}, \frac{\Delta^-_x\Delta^+_x\psi_{i\pm1,j}}{h}, \frac{\Delta^-_x\Delta^+_x\psi_{i,j}}{h}, \frac{\Delta^-_x\Delta^+_x\psi_{i\mp1,j}}{h}\right) \text{ and} \end{aligned} \tag{2.14}$$

$$\begin{aligned} \psi^{\pm}_{y\,i,j} &= \frac{1}{12\,h}\left(-\Delta^+_y\psi_{i,j-2} + 7\Delta^+_y\psi_{i,j-1} + 7\Delta^+_y\psi_{i,j} - \Delta^+_y\psi_{i,j+1}\right) \\ &\quad \pm\Phi^{\text{WENO}}\left(\frac{\Delta^-_y\Delta^+_y\psi_{i,j\pm2}}{h}, \frac{\Delta^-_y\Delta^+_y\psi_{i,j\pm1}}{h}, \frac{\Delta^-_y\Delta^+_y\psi_{i,j}}{h}, \frac{\Delta^-_y\Delta^+_y\psi_{i,j\mp1}}{h}\right), \end{aligned} \tag{2.15}$$

where

$$\Phi^{\text{WENO}}(a,b,c,d) = \frac{1}{3}w_0(a - 2b + c) + \frac{1}{6}\left(w_2 - \frac{1}{2}\right)(b - 2c + d). \tag{2.16}$$

The weights w_0 and w_2 are given by

$$w_0 = \frac{\alpha_0}{\alpha_0 + \alpha_1 + \alpha_2} \text{ and } w_2 = \frac{\alpha_2}{\alpha_0 + \alpha_1 + \alpha_2},$$

where

$$\alpha_0 = \frac{1}{(IS_0 + \epsilon_1)^2},\ \alpha_1 = \frac{6}{(IS_1 + \epsilon_1)^2},\ \alpha_2 = \frac{3}{(IS_2 + \epsilon_1)^2},$$

$$IS_0 = 13(a-b)^2 + 3(a-3b)^2,\ IS_1 = 13(b-c)^2 + 3(b+c)^2, \text{ and } IS_2 = 13(c-d)^2 + 3(3c-d)^2.$$

In the above expressions, ϵ_1 has been used just to avoid the division by zero. Following [7] we take it to be 10^{-6}.

2.1.2 Boundary integrals

The expression for misorientation (denoted by θ) evolution during the coupled GB motion involves line integrals over the whole GB. Additionally, the area enclosed by the GB (denoted by A) is given in terms of an integral over the domain ω^+. There are two ways to evaluate these integrals. We can trace the actual position of the GB (the zero level set) by interpolation, and then numerically evaluate the integrals by discretizing the closed curve into small arc lengths. However the interpolations used to capture C introduce errors in the computation. This problem can be avoided if we evaluate the integrals implicitly in the form

$$\int_\omega f(\boldsymbol{x})\delta(\psi(\boldsymbol{x}))||\nabla\psi(\boldsymbol{x})||da, \tag{2.17}$$

which is same as $\int_C f(\boldsymbol{x})\, ds$ (cf. §1.5 of [9]). In the above integral $\delta(\psi(\boldsymbol{x}))$ is the Dirac delta generalized function. Similarly, an area integral over the inner grain ω^+ can be calculated using

$$\int_\omega f(\boldsymbol{x})H(\psi)da, \tag{2.18}$$

where $H(\psi)$ is a one dimensional Heaviside function. We use the following approximate functional form to represent the Heaviside function (see §1.5 of [9]):

$$H(\psi) = \begin{cases} 0, & \text{if } \psi < -\epsilon \\ \frac{1}{2} + \frac{\psi}{2\epsilon} + \frac{1}{2\pi}\sin(\frac{\pi\psi}{\epsilon}), & \text{if } |\psi| \le \epsilon \\ 1, & \text{if } \psi > \epsilon, \end{cases} \tag{2.19}$$

where $0 < \epsilon \ll 1$. We use the following first order accurate Dirac delta function for computing the boundary integrals [15]:

$$\delta(\psi_{i,j}) = \delta_{i,j}^{(+x)} + \delta_{i,j}^{(-x)} + \delta_{i,j}^{(+y)} + \delta_{i,j}^{(-y)}, \tag{2.20}$$

where

$$\delta_{i,j}^{(+x)} = \begin{cases} \frac{|\psi_{i+1,j} D_x^0 \psi_{i,j}|}{h^2 |D_x^+ \psi_{i,j}||\nabla_0 \psi_{i,j}|}, & \text{if } \psi_{i,j}\psi_{i+1,j} \leq 0, \\ 0, & \text{otherwise,} \end{cases}$$

$$\delta_{i,j}^{(-x)} = \begin{cases} \frac{|\psi_{i-1,j} D_x^0 \psi_{i,j}|}{h^2 |D_x^- \psi_{i,j}||\nabla_0 \psi_{i,j}|}, & \text{if } \psi_{i,j}\psi_{i-1,j} < 0, \\ 0, & \text{otherwise,} \end{cases}$$

$$\delta_{i,j}^{(+y)} = \begin{cases} \frac{|\psi_{i,j+1} D_y^0 \psi_{i,j}|}{h^2 |D_y^+ \psi_{i,j}||\nabla_0 \psi_{i,j}|}, & \text{if } \psi_{i,j}\psi_{i,j+1} \leq 0, \\ 0, & \text{otherwise,} \end{cases}$$

$$\delta_{i,j}^{(-y)} = \begin{cases} \frac{|\psi_{i,j-1} D_y^0 \psi_{i,j}|}{h^2 |D_y^- \psi_{i,j}||\nabla_0 \psi_{i,j}|}, & \text{if } \psi_{i,j}\psi_{i,j-1} < 0, \\ 0, & \text{otherwise;} \end{cases}$$

$D_x^+ \psi_{i,j} = \frac{\psi_{i+1,j} - \psi_{i,j}}{h}$, $D_x^- \psi_{i,j} = \frac{\psi_{i,j} - \psi_{i-1,j}}{h}$, $D_x^0 \psi_{i,j} = \frac{\psi_{i+1,j} - \psi_{i-1,j}}{2h}$, $D_y^+ \psi_{i,j}$, $D_y^- \psi_{i,j}$, $D_y^0 \psi_{i,j}$ are computed in a similar way, and $|\nabla_0 \psi_{i,j}| = \sqrt{(D_x^0 \psi_{i,j})^2 + (D_y^0 \psi_{i,j})^2 + \epsilon_2}$, with ϵ_2 taken to be 10^{-10}.

2.1.3 Normal velocity

We now shift our focus to the discretization of the normal velocity associated with the grain boundary. This involves computing the weighted curvature and the surface Laplacian of the mean curvature inside the tube T_1.

Divergence of $\boldsymbol{\xi}$ Using (2.1) and (2.2) in (1.3) and taking a divergence, we write

$$\nabla \cdot \boldsymbol{\xi} = \nabla \cdot (\gamma_c \boldsymbol{n} - \gamma_c' \boldsymbol{t}) = \frac{\partial}{\partial x}\left(\gamma_c \frac{\partial \psi/\partial x}{||\nabla \psi||} - \gamma_c' \frac{\partial \psi/\partial y}{||\nabla \psi||}\right) + \frac{\partial}{\partial y}\left(\gamma_c \frac{\partial \psi/\partial y}{||\nabla \psi||} + \gamma_c' \frac{\partial \psi/\partial x}{||\nabla\, \psi||}\right). \quad (2.21)$$

To discretize (2.21), we invoke the following spatial discretization scheme of Cecil and Osher [3] with a compact stencil

$$\begin{aligned}(\nabla \cdot \boldsymbol{\xi})_{i,j} = \frac{1}{h}\Bigg[&\left(\gamma_c \frac{\partial \psi/\partial x}{||\nabla \psi||} - \gamma_c' \frac{\partial \psi/\partial y}{||\nabla\, \psi||}\right)_{i+1/2,j} - \left(\gamma_c \frac{\partial \psi/\partial x}{||\nabla \psi||} - \gamma_c' \frac{\partial \psi/\partial y}{||\nabla \psi||}\right)_{i-1/2,j} \\ &+ \left(\gamma_c \frac{\partial \psi/\partial y}{||\nabla \psi||} + \gamma_c' \frac{\partial \psi/\partial x}{||\nabla \psi||}\right)_{i,j+1/2} - \left(\gamma_c \frac{\partial \psi/\partial y}{||\nabla \psi||} + \gamma_c' \frac{\partial \psi/\partial x}{||\nabla \psi||}\right)_{i,j-1/2}\Bigg], \end{aligned} \quad (2.22)$$

where

$$(\partial\psi/\partial x)_{i+1/2,j} = (\psi_{i+1,j} - \psi_{i,j})/h,\ (\partial\psi/\partial y)_{i+1/2,j} = (\psi_{i+1,j+1} - \psi_{i+1,j-1} + \psi_{i,j+1} - \psi_{i,j-1})/4h,$$

$$(\partial\psi/\partial x)_{i-1/2,j} = (\psi_{i,j} - \psi_{i-1,j})/h,\ (\partial\psi/\partial y)_{i-1/2,j} = (\psi_{i,j+1} - \psi_{i,j-1} + \psi_{i-1,j+1} - \psi_{i-1,j-1})/4h,$$

$$(\partial\psi/\partial x)_{i,j+1/2} = (\psi_{i+1,j+1} - \psi_{i-1,j+1} + \psi_{i+1,j} - \psi_{i-1,j})/4h,\ (\partial\psi/\partial y)_{i,j+1/2} = (\psi_{i,j+1} - \psi_{i,j})/h,$$

$$(\partial\psi/\partial x)_{i,j-1/2} = (\psi_{i+1,j} - \psi_{i-1,j} + \psi_{i+1,j-1} - \psi_{i-1,j-1})/4h, \text{ and } (\partial\psi/\partial y)_{i,j-1/2} = (\psi_{i,j} - \psi_{i,j-1})/h.$$

The GB energy γ_c and its derivative γ_c' are functions of $\phi = \tan^{-1}(n_2/n_1)$, where $n_1 = \boldsymbol{n}\cdot\boldsymbol{e}_1$ and $n_2 = \boldsymbol{n}\cdot\boldsymbol{e}_2$. The components of the normal at the grid point $(i+1/2, j)$ are calculated using $(n_1)_{i+1/2,j} = (\psi_x)_{i+1/2,j}/||\nabla\psi||_{i+1/2,j}$ and $(n_2)_{i+1/2,j} = (\psi_y)_{i+1/2,j}/||\nabla\psi||_{i+1/2,j}$. The mean curvature can be computed from (2.21) by setting $\gamma_c = 1$ and $\gamma_c' = 0$. Anisotropic kinetic coefficients can be computed using the ϕ as calculated above.

Computation of $\Delta^S\kappa$ Note that $\Delta^S\kappa$ contains second order derivatives of κ in x and y, whose computation is highly sensitive to errors in ψ and κ. Following Smereka [14], we write the surface Laplacian term as

$$\Delta^S\kappa = \text{trace}\{\mathbb{P}\nabla(\mathbb{P}\nabla\kappa)\} = \frac{\partial A}{\partial x} + \frac{\partial B}{\partial y} - n_1(\boldsymbol{n}\cdot\nabla A) - n_2(\boldsymbol{n}\cdot\nabla B), \tag{2.23}$$

where $A = (\partial\kappa/\partial x) - n_1(\boldsymbol{n}\cdot\nabla\kappa)$, and $B = (\partial\kappa/\partial y) - n_2(\boldsymbol{n}\cdot\nabla\kappa)$. The spatial derivatives of κ, A, and B are computed using the central difference scheme:

$$(\psi_x)_{i,j} = (\psi_{i+1,j} - \psi_{i-1,j})/2h \text{ and } (\psi_y)_{i,j} = (\psi_{i,j+1} - \psi_{i,j-1})/2h. \tag{2.24}$$

Once the weighted curvature, mean curvature, and the Laplacian of mean curvature are known, the kinetic relations can be easily calculated (see the main paper).

2.1.4 Extension of quantities

We find the first order upwind scheme in space and the forward Euler time integration sufficient for our purposes to deal with extension of various quantities. The discrete version of (2.7) is obtained as [11]

$$\begin{aligned} q_{i,j}^{n+1} = q_{i,j}^n - \Delta t \Bigg[&(\mathcal{S}_{i,j}(n_1)_{i,j})^+ \left(\frac{q_{i,j} - q_{i-1,j}}{h}\right) + (\mathcal{S}_{i,j}(n_1)_{i,j})^- \left(\frac{q_{i+1,j} - q_{i,j}}{h}\right) \\ &+ (\mathcal{S}_{i,j}(n_2)_{i,j})^+ \left(\frac{q_{i,j} - q_{i,j-1}}{h}\right) + (\mathcal{S}_{i,j}(n_2)_{i,j})^- \left(\frac{q_{i,j+1} - q_{i,j}}{h}\right)\Bigg], \end{aligned} \tag{2.25}$$

where $(a)^+ = \max(a, 0)$, and $(a)^- = \min(a, 0)$. The sign function has been approximated as $\mathcal{S} = \psi/\sqrt{\psi^2 + h^2}$, and the components of the normal vector are computed from (2.1) using the central difference scheme given by (2.24).

2.1.5 Reinitialization

According to Russo and Smereka [12], the first order discretization in spatial derivative of the reinitialization equation (2.8) shifts the zero level set, leading to a change in its shape. This can have a considerable effect on the final results. To avoid this problem, we use the fifth order WENO scheme (described above) for spatial discretization in the reinitialization equation. This higher order scheme eliminates all the problems pointed out in [12]. The semi-discrete version of (2.8) will be the same as (2.10), but with $L = -(\text{sign}(d_i))(||\nabla d|| - 1)$ having the following discrete form

$$L_{i,j} = -[\max(\text{sign}(d_i)_{i,j}^+, 0)(||\nabla^+ d||_{i,j} - 1) + \min(\text{sign}(d_i)_{i,j}^-, 0)(||\nabla^- d||_{i,j} - 1)], \tag{2.26}$$

where $||\nabla^+(\cdot)||_{i,j}$ and $||\nabla^-(\cdot)||_{i,j}$ are given in (2.12), and

$$\text{sign}(d_i)^{\pm} = \frac{d_i}{\sqrt{d_i^2 + ||\nabla^{\pm} d_i||^2 h^2}}. \tag{2.27}$$

2.1.6 Time integration scheme

The semi-discrete equation (2.10) is integrated using the third order total variation diminishing (TVD) Runge-Kutta scheme [9]. In this scheme the level set is first advanced to time $t^n + \Delta t$, using the Euler Method, to obtain

$$\psi^{n+1} = \psi^n + \Delta t L^n \tag{2.28}$$

and then ψ^{n+1} is advanced to time $t^n + 2\Delta t$ to yield

$$\psi^{n+2} = \psi^{n+1} + \Delta t L^{n+1}. \tag{2.29}$$

Averaging the previous two steps leads to the following approximate value of ψ at time $t^n + \frac{1}{2}\Delta t$:

$$\psi^{n+1/2} = \frac{3}{4}\psi^n + \frac{1}{4}\psi^{n+2}. \tag{2.30}$$

Another Euler step is then taken to evaluate $\psi^{n+3/2}$ at time $t^n + \frac{3}{2}\Delta t$:

$$\psi^{n+3/2} = \psi^{n+\frac{1}{2}} + \Delta t L^{n+\frac{1}{2}}. \tag{2.31}$$

Finally, ψ^{n+1} is obtained by the following average:

$$\psi^{n+1} = \frac{1}{3}\psi^n + \frac{2}{3}\psi^{n+\frac{3}{2}} \tag{2.32}$$

at time $t^n + \Delta t$. This scheme has been also used for the time integration of the reinitialization equation (2.8). For the extension equation, however, we have used the forward Euler method given by (2.25). Since we are using an explicit time integration, Δt must satisfy the Courant-Friedrichs-Lewy (CFL) condition (cf. Ch. 3 in [9]) given by

$$\Delta t < h/\max(|V|). \tag{2.33}$$

The CFL condition for (2.5), in the presence of $\Delta^S \kappa$, yields $\Delta t \sim h^4$ [4].[2]

2.1.7 Summary

We now summarize the overall computational algorithm.

(i) Initialize ψ and θ: Initialize $\psi_i = \psi(\boldsymbol{x}, 0)$ as an SDF. If ψ_i is not an SDF, apply the reinitialization equation (2.8) to convert it to an SDF in the domain of computation. Also initialize θ during the coupled GB motion.

[2] We took $\Delta t = 0.5\, h^4$ to avoid numerical instabilities in our computations.

(ii) Construct computational tubes: Construct two computational tubes T_1 and T_2 surrounding the zero level set such that $|\psi_i| \leq c_1$ in T_1 and $|\psi_i| \leq c_2$ in T_2. We have taken $c_1 = 2h$ and $c_2 = 4h$, where h is the mesh size. We also construct a third tube $T_3 = \{\boldsymbol{x} : \psi_i(\boldsymbol{x} + \boldsymbol{\delta}) < c_2, \text{ for } |\boldsymbol{\delta}| < h\}$ [11]. The tube T_3 contains T_2 and the grid points which are just adjacent to T_2.

(iii) Constitutive relations: Compute γ, M, S, and β as functions of θ and ϕ.

(iv) Computations of κ and $\Delta^S\kappa$: Start with computing κ and $\nabla \cdot \boldsymbol{\xi}$ within tube T_1 and then extend these quantities into $T_2 \backslash T_1$ using extension equation (2.25). Similarly, wherever $\Delta^S\kappa$ is present, we first discretize it over T_1 using the scheme described above, and then extend it to $T_2 \backslash T_1$. For solving the extension equations, we have taken $\Delta t = 0.6h$, and used six iterations so that the extended quantities in $T_2 \backslash T_1$ reach their steady state values.

(v) Computations of the kinetic relations: Evaluate the kinetic relations for the normal velocity and the misorientation rate using the above quantities. The computational details for calculating the boundary and the area integrals have been provided above, where we take $\epsilon = c_1$ in (2.20). Finally, V is computed inside T_1 and then extended to $T_2 \backslash T_1$.

(vi) Updating of ψ and θ: Integrate the modified Hamilton-Jacobi equation (2.5) inside T_2, along with updating θ. The time steps are to be taken appropriately for different problems while satisfying the corresponding CFL conditions.

(vii) Reinitialization: Reinitialize ψ (which was computed in step (vi)) inside region T_3 using the reinitialization equation (2.8). We have iterated the reinitialization equation once after every time update of ψ in Step (vi) by taking $\Delta t = 0.6h$.

(viii) Once the new ψ (which is an SDF) is obtained, go to step (i) and repeat the calculations.

3 Examples

We now provide several examples, which are well established in the available literature, to verify our level set code. Firstly, we reproduce the boundary diffusion results (driven by $\Delta^S\kappa$ driven) of Smereka [14] for initially elliptic and star shaped boundaries. Next, we simulate the migration of a circular GB with $\gamma_c = -1$, followed by a study of the classical Wulff problem with anisotropic boundary energy. Finally, we investigate the shape evolutions of shrinking GBs. **All the simulations, except the ones in Sec. 3.1, have been performed in a square domain** $[-1, 1] \times [-1, 1]$ **with** $N = 50$**,** $M = 1$**, and** $\delta_r = 0.01$**.**

3.1 Normal motion due to surface diffusion

The surface diffusion simulations of Smereka [14], with kinetic relation given by $V = \Delta^S\kappa$, for the initial boundary geometries such as an ellipse and a seven lobbed star are reproduced. See Figure

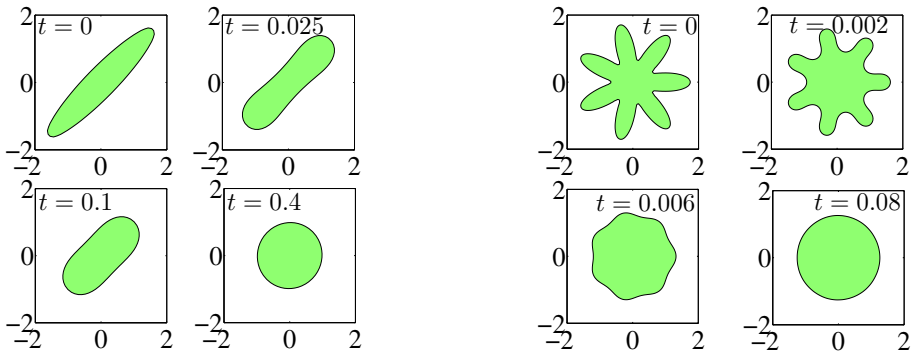

(a) (b)

Figure 3: (a) The evolution of an ellipse under surface diffusion. The initial configuration of the ellipse has the semi-major and semi-minor axes length 2.25 and 0.45, respectively; the major axis makes 45° angle with $\boldsymbol{e}_1$. For computation, we have divided a square domain $[-2.6, 2.6]\times[-2.6, 2.6]$ with $N = 50$ grid points in both the directions. (b) The initial geometry is given by $\psi_i = 1.2 + 0.55\cos(7\chi) - \sqrt{x^2+y^2}$, where $\chi = \tan^{-1}(y/x)$. The domain of computation is $[-2.4, 2.4] \times [-2.4, 2.4]$, and $N = 100$.

3(a) and 3(b), respectively, for the simulation results which are in good match with those of [14].

3.2 Migration of a circular GB with $\gamma_c = -1$

We consider the migration of an initially circular GB of radius R_i, where $\gamma_c = -1$. The kinetic equation, which is now a backward parabolic PDE everywhere, simplifies to

$$\dot{R} = \frac{M}{2R}\left(1 + \frac{\delta_r}{2R^2}\right), \tag{3.1}$$

where R is the radius of the evolving GB. Its solution is approximately given by $R \approx \sqrt{R_i^2 + 2M(1+\delta_r/2R^2)t}$, where the regularity term has been assumed to be constant. The second term in the parenthesis is at least two order of magnitudes smaller than unity when $\delta_r = 0.01$ and $R(t)$ is of the same order as R_i. Without loosing any accuracy in the solution, we can therefore replace R by R_i in the denominator of the regularity term in the solution. According to our level set simulations, the initial circular profile only increases in size without changing its shape. The approximate analytical solution and the level set result are in very good agreement, as shown in Figure 4, where the maximum difference between two solutions is less than 1%.

3.3 Wulff problem

Wulff problem is a classical constrained optimization problem which includes solving for the optimal shape of an isolated crystalline grain such that the total interfacial energy is minimized. For the

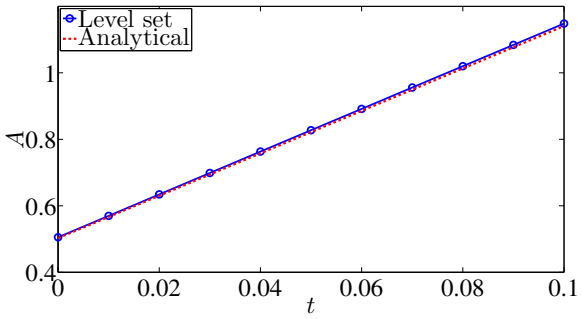

Figure 4: Area evolution of a circular GB with $R_i = 0.4$ and $\gamma_c = -1$.

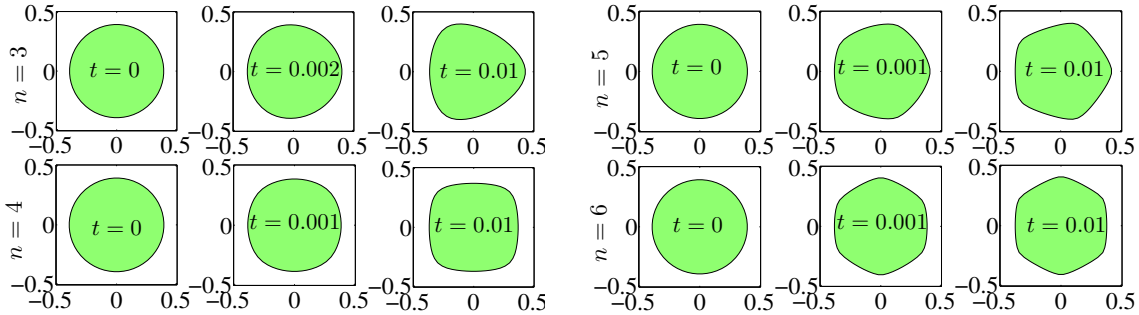

(a) (b)

Figure 5: Evolution of Wulff crystals from a circle when (a) $n = 3$ (first row), 4 (second row), and (b) $n = 5$ (first row), 6 (second row) in (1.4). The computations have been performed with $\alpha_e = 0.25$. The shapes do not evolve significantly beyond the time instances indicated in the final figure of the respective rows.

level set simulations of the Wulff problem, we adopt the method of Cecil and Osher [3]. The method requires solving (2.5) for ψ (V is given by (1.2)), and then adding λ to ψ after every time update, where λ is computed by expanding the area constraint

$$\int_\omega H(\psi(\boldsymbol{x}) + \lambda) da = A_i \tag{3.2}$$

in Taylor series about ψ and then making use of a first order approximation. Hence

$$\lambda = \frac{A_i - \int_\omega H(\psi) da}{\int_\omega \delta(\psi) ||\nabla \psi|| da}. \tag{3.3}$$

Figures 5(a) and 5(b) present evolution of isolated circular crystals, with anisotropic boundary energy given by (1.4), towards the equilibrium shapes. The facets are formed according to the angles in γ_c plot for which the energy has a local minima. The corners correspond to those angles for which the stiffness $\gamma_c + \gamma_c''$ is negative. Such angular ranges are called surface spinodals (or interfacial spinodal in case of an interface), due to their similarity with the spinodals in the Cahn-Hilliard theory

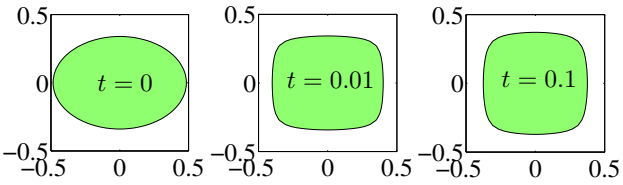

Figure 6: Wulff shape of an initially elliptical crystal with free boundary. We have taken $\alpha_e = 0.25$ and $n = 4$.

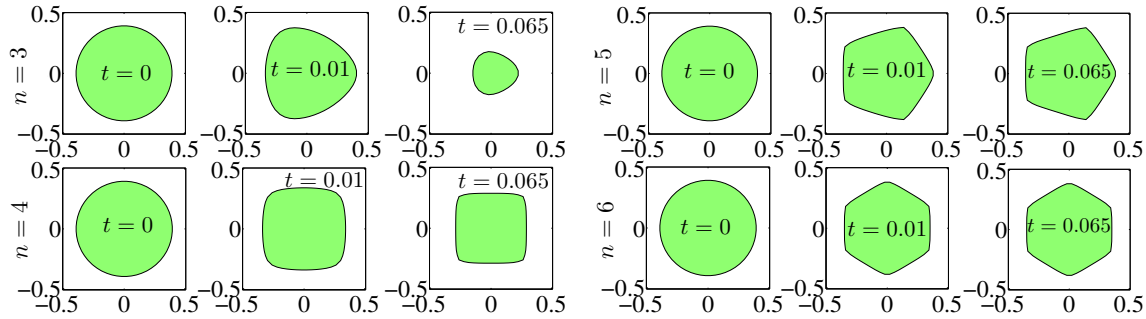

(a) (b)

Figure 7: (a) Evolution of initially circular GB when (a) $n = 3$ (first row), 4 (second row), and (b) $n = 5$ (first row) and 6 (second row) in (1.4). We have taken $\alpha_e = 0.25$.

of phase transformations [2]. It is not necessary that all non-convex surface energy will have spinodals. For example, if a smooth and non-convex energy is given by (1.4) with $n = 4$ and $\alpha_e \lesssim 0.067$, then the surface stiffness is non-negative for all $0 \leq \phi < 2\pi$. Whether a surface energy of a form (1.4) will contain a spinodal or not, is governed by α_e. However a smooth and non-convex energy, which does not have any spinodal, will still force the crystals to attain the corresponding Wulff shapes, since the inclinations corresponding to the lower energies will be preferred over the inclinations with higher energies. Hence the shape of the crystal will contain faces with small curvatures, connected with smooth corners. In crystalline materials, the surface energy (or the interfacial energy) is strongly anisotropic (i.e. $0 \ll \alpha_e < 1$), and hence always exhibits spinodals. This results in appearance of facets in the equilibrium shapes of crystals. In Figure 6 we obtain the expected Wulff shape starting from an elliptic crystalline grain. All the above results are consistent with the geometrical constructions of Herring [6], see also [8].

3.4 Shrinkage and shape evolution of the GBs by normal motion

Finally, we study the evolution of initially circular GBs which are governed by kinetic relation given in (1.2). We do not impose any constraint on the area thereby allowing the GBs to shrink. When a circular GB, with an anisotropic energy given by (1.4), is evolved the inner grain shrinks and eventually attains the Wulff shape as depicted in Figures 7(a) and 7(b). In all the cases, the grain

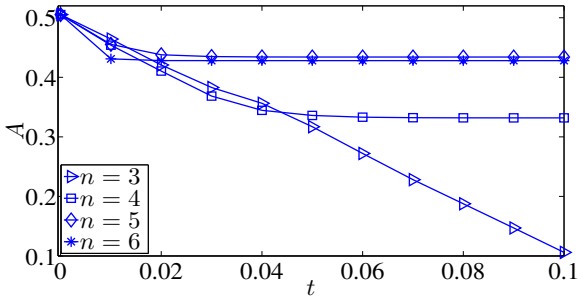

Figure 8: Area evolution of the inner grain during normal motion with non-convex energies given by (1.4). The curves represent the variation of the area A with varying n. We have taken $\alpha_e = 0.25$.

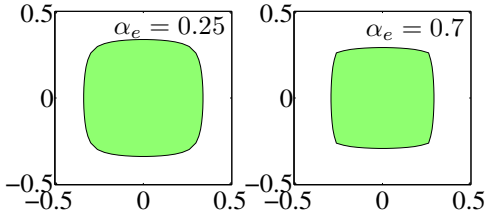

Figure 9: A comparative study of shape evolution for two different values of α_e, where $n = 4$. In both the cases the initial boundaries are circular with $R_i = 0.4$. The snapshots have been taken at $t = 0.01$.

size decays along with the evolution of the facets but eventually stabilizes at a finite size. This is clearly illustrated in Figure 8 which depicts the change in the area of the inner grain for several choices of n. According to this plot the area evolution stops after a short time period when $n > 3$, with that saturation time becoming smaller with increasing n. In Figure 9 we note that the facets appear much more rapidly for $\alpha_e = 0.7$ than for $\alpha_e = 0.25$. Moreover, the corners are also sharper. As α_e approaches 1 the smooth minimas of γ_c shown in Figure 1 become more cusp-like and hence resulting into the observed shape. Our results are in good agreement with those provided in [3, 1].

References

[1] M. Burger, F. Haußer, C. Stöcker, and A. Voigt. A level set approach to anisotropic flows with curvature regularization. *Journal of Computational Physics*, 225:183–205, 2007.

[2] A. D. Carlo, M. E. Gurtin, and P. Podio-Guidugli. A regularized equation for anisotropic motion-by-curvature. *SIAM Journal on Applied Mathematics*, 52:1111–1119, 1992.

[3] T. Cecil and S. Osher. Regularized Wulff flows, nonconvex energies and backwards parabolic equations. *ftp://ftp.math.ucla.edu/pub/camreport/cam04-09.pdf*, 2004.

[4] D. L. Chopp and J. A. Sethian. Motion by intrinsic Laplacian of curvature. *Interfaces and Free Boundaries*, 1:1–18, 1999.

[5] Y. Giga. *Surface Evolution Equations-A Level Set Approach*. Birkhäuser Verlag, Basel, 2006.

[6] C. Herring. Some theorems on the free energies of crystal surfaces. *Physical Review*, 82:87–93, 1951.

[7] G. S. Jiang and D. Peng. Weighted ENO schemes for Hamilton-Jacobi equations. *SIAM Journal on Scientific Computing*, 21:2126–2143, 2000.

[8] R. Kobayashi and Y. Giga. On anisotropy and curvature effects for growing crystals. *Japan Journal of Industrial and Applied Mathematics*, 18:207–230, 2001.

[9] S. Osher and R. Fedkiw. *Level Set Methods and Dynamic Implicit Surfaces*. Springer-Verlag, New York, 2003.

[10] S. Osher and J. A. Sethian. Fronts propagating with curvature-dependent speed: Algorithms based on Hamilton-Jacobi formulations. *Journal of Computational Physics*, 79:12–49, 1988.

[11] D. Peng, B. Merriman, S. Osher, H. Zhao, and M. Kang. A PDE-based fast local level set method. *Journal of Computational Physics*, 155:410–438, 1999.

[12] G. Russo and P. Smereka. A remark on computing distance functions. *Journal of Computational Physics*, 163:51–67, 2000.

[13] J. A. Sethian. *Level Set Methods: Evolving Interfaces in Geometry, Fluid Mechanics, Computer Vision, and Material Science*. Cambridge University Press, New York, 1996.

[14] P. Smereka. Semi-implicit level set methods for curvature and surface diffusion motion. *Journal of Scientific Computing*, 19:439–456, 2003.

[15] P. Smereka. The numerical approximation of a delta function with application to level set methods. *Journal of Computational Physics*, 211:77–90, 2006.

[16] B. J. Spencer. Asymptotic solutions for the equilibrium crystal shape with small corner energy regularization. *Physical Review E*, 69:(011603) 1–10, 2004.